Bioactive Materials 13 (2022) 200–211

Contents lists available at ScienceDirect

Bioactive Materials

journal homepage: www.keaipublishing.com/en/journals/bioactive-materials

The enhanced photocatalytic sterilization of MOF-Based nanohybrid for rapid and portable therapy of bacteria-infected open wounds

Chaofeng Wang [a], Yue Luo [a], Xiangmei Liu [b,**], Zhenduo Cui [c], Yufeng Zheng [d], Yanqin Liang [c], Zhaoyang Li [c], Shengli Zhu [c], Jie Lei [e], Xiaobo Feng [e], Shuilin Wu [a,c,*]

[a] Biomedical Materials Engineering Research Center, Collaborative Innovation Center for Advanced Organic Chemical Materials Co-constructed by the Province and Ministry, Hubei Key Laboratory of Polymer Materials, Ministry-of-Education Key Laboratory for the Green Preparation and Application of Functional Materials, School of Materials Science & Engineering, Hubei University, Wuhan 430062, China
[b] School of Life Science and Health Engineering, Hebei University of Technology, Xiping Avenue 5340, Beichen District, Tianjin 300401, China
[c] School of Materials Science & Engineering, The Key Laboratory of Advanced Ceramics and Machining Technology by the Ministry of Education of China, Tianjin University, Tianjin 300072, PR China
[d] School of Materials Science & Engineering, State Key Laboratory for Turbulence and Complex System, Peking University, Beijing 100871, China
[e] Department of Orthopaedics, Union Hospital, Tongji Medical College, Huazhong University of Science and Technology, Wuhan 430022, PR China

ARTICLE INFO

Keywords:
Antibacterial
Wound healing
Bacterial infection
MOF
Photocatalytic

ABSTRACT

Open wounds are prone to infection and difficult to heal, which even threatens the life of patients because bacterial infections can induce other lethal complications without prompt treatment. The commonly used antibiotics treatment for bacterial infections has been reported to cause globally bacterial resistance and even the occurrence of superbacteria. The highly effective and antibiotic-independent therapeutic strategies are urgently needed for treating various kinds of bacteria-infected diseases. In this work, we synthesized an eco-friendly nanohybrid material (ZnDMZ) consisting of a kind of biodegradable metal organic framework (MOF, ZIF-8) combined with Zn-doped MoS_2 (Zn–MoS_2) nanosheets, which exhibited great ability to kill bacteria and promote the healing of bacteria-infected wounds under 660 nm light irradiation. The underlying mechanism is that besides the local hyperthermia, the nanohybrid material exhibits enhanced photocatalytic performance than single component in it, *i.e.*, it can also be excited by 660 nm light to produce more oxygen radical species (ROS) due to the following factors. On one hand, the Zn doping can reduce the work function and the band gap of MoS_2, which promotes the movement of photoexcited electrons to the surface of the material. On the other hand, the combination between Zn–MoS_2 and MOF induces the formation of a built-in electric field due to their work function difference, thus accelerating the separation of photoexcited electron-hole pairs. Because of the synergy of photocatalytic effect, photothermal effect and the released Zn ions, the synthesized ZnDMZ possessed a highly effective antibacterial efficacy of 99.9% against *Staphylococcus aureus* under 660 nm light irradiation for 20 min without cytotoxicity. *In vivo* tests showed that this nanohybrid material promoted the wound healing due to the released Zn ions. This nanohybrid will be promising for rapid and portable treatment of bacteria-infected open wounds in pathogenic bacteria contaminated environments.

1. Introduction

Skin is the most important line of defense for human beings against external invasion from pathogenic microbia [1]. However, skin wounds are inevitable by various kinds of unpredictable injuries [2,3]. Although in most of cases open wounds do little harm to people, if it is not sterilized timely, pathogenic bacteria will invade the damaged tissues, which would not only impair wound healing, but also cause severe

Peer review under responsibility of KeAi Communications Co., Ltd.

* Corresponding author. Biomedical Materials Engineering Research Center, Collaborative Innovation Center for Advanced Organic Chemical Materials Co-constructed by the Province and Ministry, Hubei Key Laboratory of Polymer Materials, Ministry-of-Education Key Laboratory for the Green Preparation and Application of Functional Materials, School of Materials Science & Engineering, Hubei University, Wuhan 430062, China.
** Corresponding author.
E-mail addresses: liuxiangmei1978@163.com (X. Liu), shuilin.wu@gmail.com, shuilinwu@tju.edu.cn (S. Wu).

https://doi.org/10.1016/j.bioactmat.2021.10.033
Received 6 October 2021; Received in revised form 21 October 2021; Accepted 21 October 2021
Available online 2 November 2021

complications and even threaten people's life [4]. *Staphylococcus aureus* (*S. aureus*) is a common pathogen of skin wound infection, which often develops complications like bacterial pneumonia, osteomyelitis and so on [5,6]. Current clinical methods against bacteria associated infection are mainly antibiotic therapy [7]. Nevertheless, the abuse of antibiotics is responsible for the development of bacterial drug resistance [8]. Therefore, it's urgent to exploit a safe and reliable method for rapid antibacterial therapy. Sunlight is a green resource everywhere in nature. Taking use of sun light and its thermal effect to eliminate bacteria has shown great potential in recent years [9], in which reactive oxygen species (ROS) and hyperthermia were produced by various kinds of photoresponsive materials under light stimulation [10]. Photodynamic and photothermal therapy, without the usage of antibiotics, is able to combat drug resistant bacteria even superbugs [11]. Taking the above advantages together, strategies of designing a biocompatible, green and effective photoresponsive material occupies a core position in the field of antibacterial therapy research.

Recently, some inorganic semiconductor materials with superior light responsiveness within human body have been widely explored, examples like copper disulfide [12], bismuth disulfide [13], titanium dioxid [14] and so on. The common feature of these materials is that they can effectively separate electrons and holes under light stimulation, and therefore accelerate the downstream catalytic reaction. After capturing oxygen and water molecules from surrounding environment, the photoactivated electrons and holes can react with them to produce ROS, which is capable of killing bacteria through elevating oxidative stress and destroying the membrane structure of bacteria [15]. Besides, thanks to the photothermal nature of a few specific inorganic materials, they are able to be excited to generate heat under light irradiation, and therefore effectively elevating the local temperature [16]. The high temperature would subsequently rupture the thin bacterial membrane, destroy the integrity of the bacteria, and drive the inside structural content of the bacteria to flow out, which promotes the bacteria-killing efficiency and is named as photothermal antibacterial therapy [17,18].

With the typical graphene-like structure, two dimensional (2D) MoS_2 is characterized by large specific surface area, good photoelectric performance, narrow band gap, and good biocompatibility [19–21]. It has been frequently used in photodynamic and photothermal antibacterial therapy. However, due to the narrow band gap, the active electrons and holes generated by MoS_2 under light stimulation are easy to recombine [22]. Together with the poor oxygen absorbing ability, the antibacterial properties of pure MoS_2 are largely hampered. Therefore, it's an emergency to overcome these two shortcomings in order to improve the antibacterial effect of MoS_2 [23]. Previous studies had found that metal ions such as zinc ion and copper ions not only possessed intrinsic antibacterial property but also was beneficial for wound healing [24,25]. Especially, zinc ions dopant can effectively improve the photocatalytic performance of photo responsive materials [26,27]. ZIF-8 is a typical metal-organic framework (MOF) with intrinsic electron transport capacity, which has a large specific surface area and porosity, and can effectively absorb oxygen molecules. Additionally, this kind of MOF can gradually release Zn ions from its metallic nodes during degradation process. Zinc ions promote wound healing by upregulating the expression of genes that control tissue repair, such as Matrix metalloproteinase-2 (MMP-2) and Type III collagen (col-III) [28,29].

Based on the above analysis, we propose a hypothesis if an eco-friendly hybrid material with enhanced photocatalytic performance together photothermal effects can be designed through the combination between Zn doped MoS_2 nanosheets with ZIF-8 MOF, which could be utilized for rapid and effective bacteria-killing and accelerating wound healing simultaneously. In order to verify the hypothesis, Zn-doped MoS_2 nanosheets (Zn–MoS_2) were synthesized by a simple hydrothermal process and the followed ultrasonic solvent stripping method in the solution of $Zn(NO3)_2{\cdot}6H_2O$. The combination between Zn–MoS_2 and ZIF-8 (ZnDMZ) was carried out by a simple physical mixing process of Zn–MoS_2 solution with the solution of 2-methylimidazole in methanol. The preparation process was schematically illustrated in Scheme S1 (Supporting Information). On one hand, the Zn-doping reduces the band gap of MoS_2, making it easier to be excited by 660 nm light. On the other hand, besides providing more oxygen absorbed by its myriads of voids, ZIF-8 can transport photo-generated electrons rapidly and thus inhibit the recombination of holes and electrons, which endow this nanohybrid material with enhanced photocatalytic performance under 660 nm light irradiation. Consequently, the synthesized ZnDMZ exhibited highly effective bacteria-killing efficacy and wound healing effects due to the synergy of photocatalytic and photothermal effects as well as the released Zn ions, which was schematically illustrated in Scheme 1.

2. Experiment method

2.1. Synthesis of MoS_2

The sodium molybdate dihydrate (1.693 g) and thiourea (2.664 g) were mixed with 40 mL distilled water under vigorous stirring. When the solution became homogenous and transparent, 2 M HCl was used to adjust the pH of the solution to below 1.0. After stirring at room temperature for 2 h, the solution was transferred into 100 mL Teflon-lined stainless steel, which was then placed into a muffle furnace. The temperature was heated to 200 °C with a rate of 5 °C/min and maintained at 200 °C for 24 h. After cooling down the room temperature naturally, the sample was collected by centrifugation with 9000 r/min, washed by distilled water and absolute ethyl alcohol successively for several times, and finally dried in an oven at 60 °C for 12 h for further use.

2.2. Synthesis of ZIF-8

Firstly, the 2.389 g $Zn(NO3)_2{\cdot}6H_2O$ was dissolved into 100 mL methanol, and the solution was named A. Meanwhile, 2.77 g of 2-methylimidazole was dissolved into 100 mL methanol solution, which was named B. And then the solution B was added into A drop by drop with continuously stirring for 4 h. After that, the sample of ZIF-8 was separated by centrifugation and washed with methanol and distilled successively for several times and finally dried in an oven at 60 °C for 6 h for further use.

2.3. Synthesis of Zn-doped MoS_2 (Zn–MoS_2) and Zn–MoS_2-ZIF-8 (ZnDMZ)

In order to obtain the materials of Zn–MoS_2 and ZnDMZ, 2 g of prepared MoS_2 was dissolved in 100 mL of methanol, then 0.223 g $Zn(NO3)_2{\cdot}6H_2O$ was added with the continuously stirring for 12 h under ultrasonic, which was named the solution C. During ultrasonic stripping process, zinc ions in the solution were partially doped into the nanosheets, and some of zinc ions were free in the solvent. After centrifugally drying, the product of Zn–MoS_2 was collected. Next, 0.693 g of 2-methylimidazole was dissolved into 100 mL methanol solution, which was named the solution D. In the next step, the solution D was added into C drop by drop with continuously stirring for 4 h, and then washed and centrifuged several times with methanol and distilled, finally dried in oven at 60 °C for 6 h. The product of ZnDMZ was collected.

2.4. Characterization

In order to examine the microstructures and morphologies of the synthesized samples, the filed-emission scanning electron (FE-SEM,7JSM1007) and transmission electron microscopy (TEM, JEOL-2100F, Japan) were utilized. X-ray diffraction was determined by a Bruker diffractometer (D8A25, Germany) with Cu Kα radiation for 2θ from 10° to 80°. The x-ray photoelectron spectroscopy (Thermo Fisher Scientific 250Xi) was used to detect the elemental compositions of the materials. Ultraviolet–visible (UV–vis) diffuse reflection spectra were obtained using a UV-3600 spectrophotometer (Shimadu, Japan).

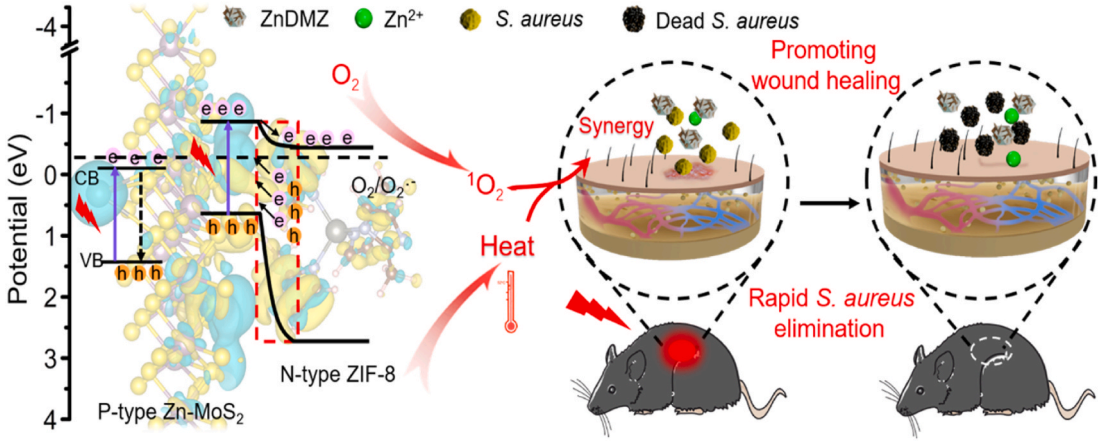

Scheme 1. The schematic illustration of ZnDMZ P–N heterojunction catalyst and antibacterial mechanism diagram of heterojunction under 660 nm light irradiation. Driven by the interface electric field and band offset at the heterointerface enable the photoexcited electrons to be separated effectively, thus increasing the production of reactive oxygen species (ROS). Under the synergistic action of ROS and heat, bacteria can be effectively eliminated to promote wound healing.

Inductively-coupled plasma atomic emission spectrometry (ICP-AES) was conducted with an Optimal 8000 instrument (PerkinElmer, US). Room temperature photoluminescence (PL) measurements were performed by a fluorescence spectrometer (LS-55, PE, USA).

2.5. Photoelectrochemical measurements

The photoelectrochemical measurements of all the samples were analyzed with a three-electrode CHI 660E electrochemical workstation, wherein platinum was used as the counter electrode and Ag/AgCl electrode served as the reference electrode. 660 nm laser with 0.45 W/cm^2 was utilized as the light source and $NaSO_4$ (0.5 M) solution was used as the electrolyte. To fabricate the working electron, 1 mL distilled water, 5 mg synthesized materials and 50 μL Nafion were fully mixed. Then, 100 μL mixed solution was dropped on the titanium plate and dried for further use. The photocurrent density was measured under alternate changes of 660 nm (0.45 W/cm^2)light irradiation and no-light irradiation. The electrochemical impedance spectroscopy (EIS) spectra were detected in the range from 100 kHz to 0.01 Hz, with an amplitude of 10 Mv under 660 nm (0.45 W/cm^2) light irradiation.

2.6. ROS detection

In order to detect the ROS production of the materials under 660 nm (0.45 W/cm^2) light irradiation, the ROS Assay Kit of 2′,7′-dichlorofluorescein (DCFH) was used, which can react with ROS to produce fluorescence that can be detected by a microplate reader. Firstly, 100 μL prepared DCFH solution was added to the 96-well plate, and then 0.4 mg/mL aqueous solution of the material was transferred into the well. The yields of ROS were checked every 2 min. The production of $^1O_2$ under visible light irradiation was usually measured by the 1,3-diphenylisobenzofuran (DPBF). When $^1O_2$ was produced, the intensity of the peak at 420 nm would decrease, which was recorded by a microplate reader.

2.7. Photothermal tests

0.2 mg/mL PBS solution of samples (MoS_2, ZIF-8, Zn–MoS_2, and ZnDMZ) was prepared separately. Then 1 mL solution was added into the 1.5 mL centrifuge tube and then treated with or without 660 nm (0.45 W/cm^2) light. The temperature was recorded every 2 min with a total of 10 time points. And then the heating–cooling cycle curves of samples were obtained.

2.8. DFT calculation

The molecular dynamics calculation of samples was calculated in the Vienna ab initio simulation package (VASP). All-electron plane-wave basis sets with an energy cutoff of 520 eV, and a projector augmented wave (PAW) method were adopted. A (3 × 3 × 1) Monkhorst-Pack mesh was used for the Brillouin-zone integrations to be sampled. The conjugate gradient algorithm was used in the optimization. The convergence threshold was set 1×10^{-4} eV in total energy and 0.05 eV/Å in force on each atom.

The adsorption energy change (ΔEabs) was determined as follows:

$$\Delta E_{abs} = E_{total} - E_{slab} - E_0$$

Where E_{total} is the total energy for the adsorption state, E_{slab} was the energy of pure surface, E_0 was the energy of O_2.

2.9. Antibacterial tests

In order to evaluate the antibacterial activity of the synthesized materials, we conducted a biological antibacterial experiment. *S. aureus* (ATCC 25923) was selected as the experiment bacterial. The changes of bacterial colonies were visually observed through spread plate method. Firstly, liquid nutrient medium was used to dilute the bacteria to 10^5 FU mL^{-1} for further use. And then one group of the samples (the Control, MoS_2, ZIF-8, Zn–MoS_2, ZnDMZ) was treated without light irradiation, while another group was irradiation under 660 nm (0.45 W/cm^2) light. All the samples were diluted with PBS to 0.8 mg/mL 50 μL bacterial solution was added into the 96 well plates, and then 150 μL PBS solution of samples was added into the plate. After irradiation for 20 min, 20 μL mixed solution was evenly coated on the agar plate, and then incubated in an oven at 37 °C for 24 h.

2.10. Bacterial morphology

The bacteria interacted with the material completely for 2 h, then the upper layer solution was removed and washed with PBS for 3 times. The glutaraldehyde was then added and placed in a dark environment for 2 h. After that, the glutaraldehyde solution was removed and washed 3 times with PBS. Then the bacteria were dehydrated with gradient alcohol (10%, 30%, 50%, 70%, 90%, 100%) successively for 15 min. The fixed bacteria were observed by FE-SEM.

2.11. Cytocompatibility evaluation

The NIH-3T3 cells were used as the target cells to evaluate the

cytotoxicity of the synthesized materials. The 3-[4,5-dimethylthiazol-2-yl]-2,5-diphenyl etrazoliumbromide (MTT) was used in this experiment. Before experiments, all materials were sterilized. After the NIH-3T3 cells were cultured in a 96-well plate for a given time, the medium was discarded. 200 μL sterilized materials (the concentration of MoS_2, ZIF-8, Zn–MoS_2, ZnDMZ were 0.2 mg/mL) were added to different well plates in sequence. After 1 day of co-cultivation, the medium was discarded, and 200 μL prepared MTT solution was added to the well plate. After incubation in a carbon dioxide incubator at 37 °C for 4 h, the liquid was discarded, and then 200 μL of DMSO solution were added into the well plate with continuously shaking for 15 min 100 μL of the supernatant was measured to obtain the absorbance (OD) at 490 nm in a microplate reader. The material and cells were irradiated with 660 nm (0.45 W/cm^2) light for 20 min and then placed in a carbon dioxide incubator at 37 °C for culturing. The other step was the same as the above.

After co-culturing for 1 day, the supernatant was removed and washed three times with the PBS. Then the 4% formaldehyde was used to immobilize the cells for 10 min. After that, the cells were stained for 30 min with FITC (YiSen, Shanghai). After washing for 3 times with PBS, DAPI (YiSen, Shanghai) was then added for 30 s to dye the cells. The images were recorded by an inverted fluorescence microscope (IFM, Olympus, IX73).

2.12. In vivo animal wound healing tests

Male Wistar rats (200–220 g body weight) were obtained from Hubei Provincial Centers for Disease Prevention and Control, and the animal experimental protocols were approved by the animal research committee of the Tongji Medical College, Huazhong University of Science and Technology, Wuhan, all of the experimental operation was conformed to the rule of the Animal Management Rules of the Ministry of Health of the People's Republic of China and the Guidelines for the Care and Use of Laboratory Animals of China. Before experiments, all rats were in good living conditions, which were divided into three groups (Control, 3 M, ZnDMZ). Then three temporal groups (2, 5, and 10 days) were set with 5 mice in each group. After anesthesia with 16% chloral hydrate (30 mg/kg), wounds model was created on the back of the rat using a tool, and then 20 μL of 10^6 CFU/mL bacterial solution was injected into the wounds along with 20 μL of either PBS (the control group and 3 M group) or 200 μg/mL of ZnDMZ (test group). After 660 nm light (0.45 W/cm^2) irradiation for 20 min, the wounds of the Control group and test group were bound with opaque sterile medical tape. The 3 M group was covered with standard 3 M wound dressing. These rats were then put into suitable surroundings to feed.

At the given time of 2, 5, 10 days, photographs were taken of the rats' wounds. After treatment of 2 days, the skin tissues on the wounds were removed and stained with Giemsa. After treatment of 10 days, the hematoxylin and eosin (H&E) staining was carried out. Heart, liver, spleen, lung and kidney tissue were collected from the sacrificed mice on the10 day post operation and stained with H&E to evaluate the toxicity of the synthesized materials.

2.13. Statistical analysis

All experiments were carried out at least three parallel groups. Data were analyzed using one-way or two-way ANOVA. $^*p < 0.05$ is considered statistically significant.

3. Results and discussion

3.1. Morphology, structure and composition of synthesized materials

The morphologies of synthesized MoS_2, ZIF-8, Zn–MoS_2, ZnDMoS_2 were shown in Figs. S1a, S1b, S1c and S1d, respectively. It can be seen that MoS_2 is composed of a lot of petaloid plates to be aggregated together. After one-step ultrasound exfoliation with Zn-doping, many nanosheets can be observed due to the ultrasound exploitation. The synthesized ZIF-8 exhibits polyhedral structure. After combination, these polyhedrons were wrapped by nanosheets. And the transmission electron microscopy (TEM) images shown in Figs. S2a–b and Fig. S3a further confirmed the observed structure of synthesized materials by scanning electron microscope (SEM). The elemental mapping images of Zn–MoS_2 detected by energy-dispersive spectroscopy (EDS) were shown in Fig. S3b, which disclosed the uniform distribution of Mo, S, Zn elements in the synthesized nanosheets, suggesting the homogeneous doping of Zn into MoS_2. TEM image (Fig. 1A) shows the core-shell structure of the synthesized ZnDMoS_2, *i.e.*, polyhedral nanoparticle of 200 nm was encapsulated by layer-like nanosheets. The EDS element mapping (Fig. 1B) shows that Mo and S are uniformly distributed on the MoS_2 nanosheets while the elements of C, N, Zn are homogeneously distributed on the plane of ZIF-8. It could be found that Zn element was not only distributed on ZIF-8, but also uniformly distributed in MoS_2 nanosheets, further suggesting the successful doping of Zn into the MoS_2. As shown in Table S1 in the Supporting Information, the atomic proportion of zinc ion in ZnDMZ is about 7.96%. Furthermore, the interface microstructure of the synthesized ZnDMZ was examined by high resolution TEM (HRTEM) (Fig. 1C). There's a clear dividing line on the interface between ZIF-8 and Zn–MoS_2. The observed (002) crystal plane belonged to MoS_2 with a lattice spacing of 6.02 Å marked by the yellow dotted line and the lattice spacing of 2.70 Å was assigned to the (100) crystal plane of MoS_2 [30,31]. The area marked in the red box was indexed to the (100) crystal face of MoS_2. It can be clearly seen that the crystal lattice of MoS_2 has been deformed, which is caused by the doping of zinc ion [13,32]. Due to the special structure of ZIF-8, it shows a non-lattice state under high magnification TEM [33]. Fig. 1D schematically illustrated the synthesis process of ZnDMZ heterojunction in atomic structure by combination of Zn–MoS_2 and ZIF-8. The doped Zn atom was located in the crystal clearance of MoS_2, in the form of bond of S–Zn, which the structure model is given by density functional theory (DFT) calculation. The density functional theory (DFT) calculation confirmed the ZIF-8 possessed a structure formed by the Zn-chelated imidazole ring at the central node, which has a strong electrostatic force with Zn-doped MoS_2 and can form a tight connection. XRD patterns (Fig. S4) exhibited the peaks located at 14.3°, 33.8°, and 58.78°, corresponding to the typical crystal planes of (002), (100) and (110) of MoS_2 [20,32], which also existed in Zn–MoS_2, and ZnDMZ, suggesting that Zn-doping and combination with ZIF-8 did not change the phase structure of MoS_2. In addition, the phase of ZIF-8 occurred in the ZnDMZ (marked by red diamond assigned to ZIF-8) [33], further suggesting the successful combination of ZIF-8 and MoS_2. The surface Zeta potential measurement (Fig. S5) suggested that the Zn–MoS_2 were more positive than the MoS_2, indicating that the zinc was doped the MoS_2. The synthesized ZnDMZ exhibited lower potential due to the chelation of partial Zn^{2+} on the surface of Zn–MoS_2 with 2-methylimidazole to form ZIF-8.

X-ray photoelectron spectroscopy (XPS) spectra were detected to verify the effects of Zn-doping and the followed combination on the valence state of elements in the synthesized materials. As shown in Fig. 2A, the survey scan of the ZnDMZ (blue curve) indicated the existence of the diffraction peaks of S, Mo, Zn, C and N. The diffraction peaks of S and Mo existed in pure MoS_2 (black curve). After MoS_2 doped with Zn (pink curve), there were diffraction peaks of not only S and Mo, but also Zn, indicating that the Zn was successfully introduced into MoS_2. The diffraction peaks contained Zn, C, N in pure ZIF-8 (the red curve). The Mo 3d XPS spectrum was shown in Fig. 2B, two peaks of MoS_2 were observed at 232.2 eV and 228.9 eV, which were Mo $2d_{3/2}$ and Mo $2d_{5/2}$, respectively, indicating that oxidation state of Mo is Mo^{4+} [34,35]. The small peaks of existence of 225.9 eV belongs to S 2s orbital. In contrast, Mo 3d and S 2s binding energies of Zn– MoS_2 are red-shifted to lower binding energies compared with MoS_2, indicating Zn doped could be arouse electron transfer form Zn to Mo, which is due to the difference in electronegativity between Mo (2.16) and Zn (1.65) atoms. Furthermore,

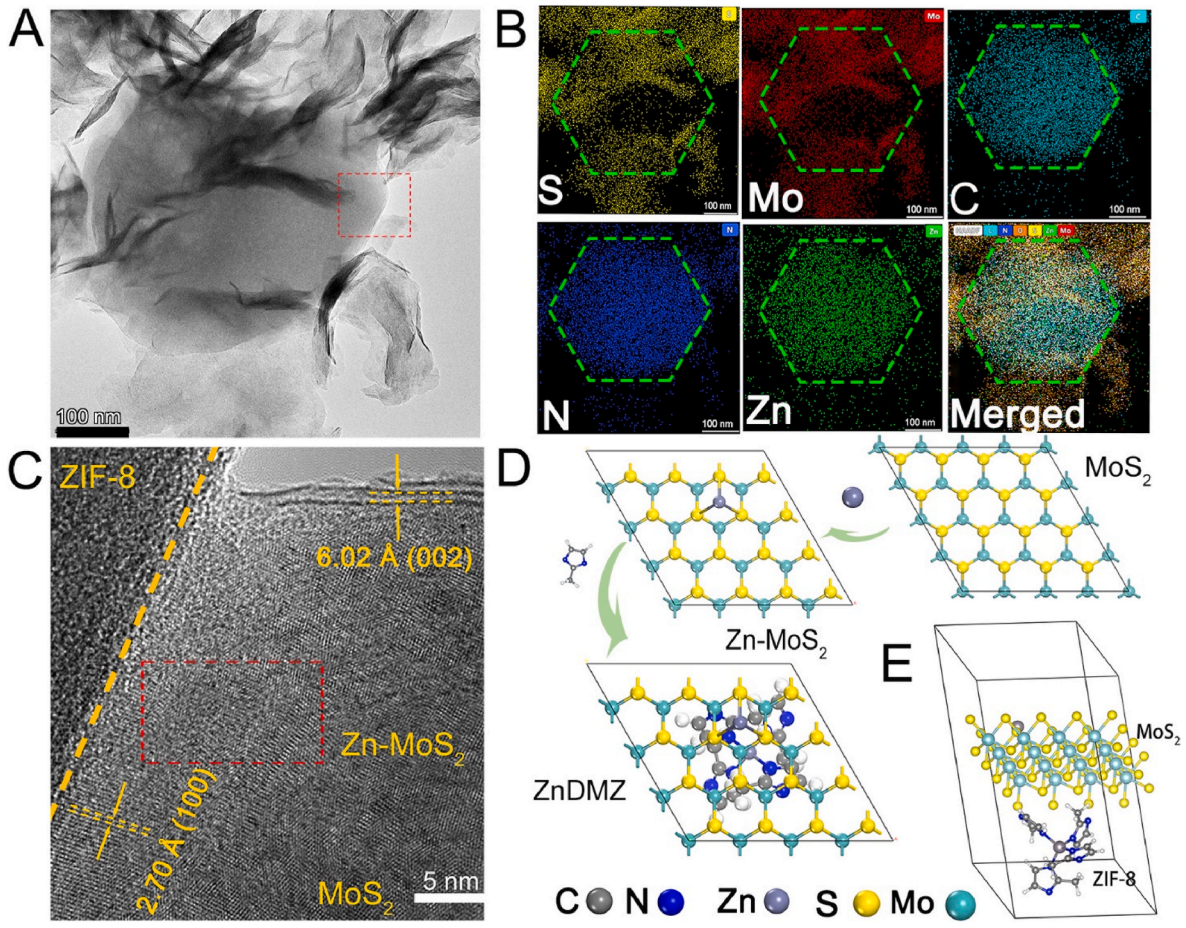

Fig. 1. (A) Morphology and structural characterization tested by TEM of ZnDMZ. (B) EDS elemental mapping of ZnDMZ (scale bar, 200 nm) (The green dotted-line marked micro-area represented the shape of ZIF-8). (C) High-resolution transmission electron microscopy (HRTEM) image of ZnDMZ. (D) Atomic schematic of the synthesis of the ZnDMZ heterojunction. (E) View of the 3D structure of ZnDMZ.

the Mo 3d spectrum of ZnDMZ further red-shift compared to Zn–MoS_2, indicating interaction between Zn–MoS_2 and MOF in ZnDMZ hybrid. Similarly, as shown in S 2p (Fig. 2C), S $2p_{1/2}$ (162.9 eV) and S $2p_{3/2}$ (161.69 eV) peaks of MoS_2 in Zn–MoS_2 are tested at lower binding energies than MoS_2, which was the difference in electronegativity between S and Zn, the electron cloud density around S decreases. In the ZnDMZ, the formation of heterojunction leads to the interaction between Zn–MoS_2 and ZIF-8, which further leads to the red shift of S2p orbitals. Zn 2p at 1044.8 eV and 1021.6 eV (Fig. 2D) appears in ZIF-8 and Zn–MoS_2 confirmed the Zn doped in MoS_2 successful. For ZnDMZ, the diffraction peaks of Zn 2p comes from ZIF-8 and the doped of Zn. In the C 1s XPS spectrum, the diffraction peak at 284.6 eV of ZIF-8 (Fig. S6a) and ZnDMZ (Fig. S7a) was the sp^2-hybridized carbon (C–C). And in N 1s of ZIF-8 (Fig. S6b) and ZnDMZ (Fig. S7b), diffraction peaks in 398.48 eV are pyridinic N [36].

3.2. Photocatalytic and photothermal performance

Fig. 3A showed the UV–Vis absorption spectra of the synthesized materials. Obviously, ZIF-8 (red curve) had almost no absorption at 660 nm light and the MoS_2 (black curve) showed a significant enhancement at wavelength of 660 nm. Zn-doping promoted the light absorption of MoS_2 (pink curve). Compared to other groups, the synthesized ZnDMZ exhibited the strongest absorption (blue curve). The separation and recombination rate of photogenerated electrons of the synthesized materials was evaluated by photoluminescence (PL) spectra. As shown in Fig. 3B, under 325 nm light excitation, the intensity of absorption peak detected form ZnDMZ was the lowest, followed by Zn–MoS_2 and MoS_2. ZIF-8 showed the highest intensity. These results suggested that the synthesized ZnDMZ had the lowest recombination rate of photogenerated electron-hole pairs. Fig. 3C showed the photocurrent densities of the prepared materials under 660 nm light irradiation. Among four kinds of materials, ZnDMZ had the strongest photocurrent density followed by Zn–MoS_2, MoS_2 and ZIF-8, indicating the best transfer ability of charge carriers of ZnDMZ under the excitation of 660 nm light. This result also suggested that Zn-doping improved the photocatalytic performance of MoS_2 and the combination with ZIF-8 further enhanced the photocatalytic property of the synthesized material. The electrochemical impedance spectroscopy (EIS) was utilized to determine the impedance of materials. As shown in Fig. 3D, the synthesized ZnDMZ exhibited the smallest semicircle among five kinds of groups, indicating the smallest impedance of ZnDMZ. The above photocurrent density and EIS measurement results disclosed that the formation of interface between Zn–MoS_2 and ZIF-8 reduced the impedance and promoted the fast transfer of photogenerated electrons. Total ROS yield was measured by the 2′,7′-dichlorofluorescein (DCFH). As shown in Fig. 3E, both the control (PBS) and ZIF-8 group only produced a very small amount of ROS under 660 nm light irradiation. MoS_2 showed a little higher ROS yield under the same condition. In contrast, Zn-doping significantly enhanced the ROS production of MoS_2. The combination between Zn–MoS_2 and ZIF-8 induced the most yields of ROS from the synthesized ZnDMZ under 660 nm light irradiation for 20 min, suggesting the best photocatalytic performance.

To study the types of ROS produced by ZnDMZ, the 1,3-diphenylisobenzofuran (DPBF) that can specifically react with singlet oxygen ($^1O_2$) was used to detect the yields of $^1O_2$. As shown in Fig. S8a, after 9 min

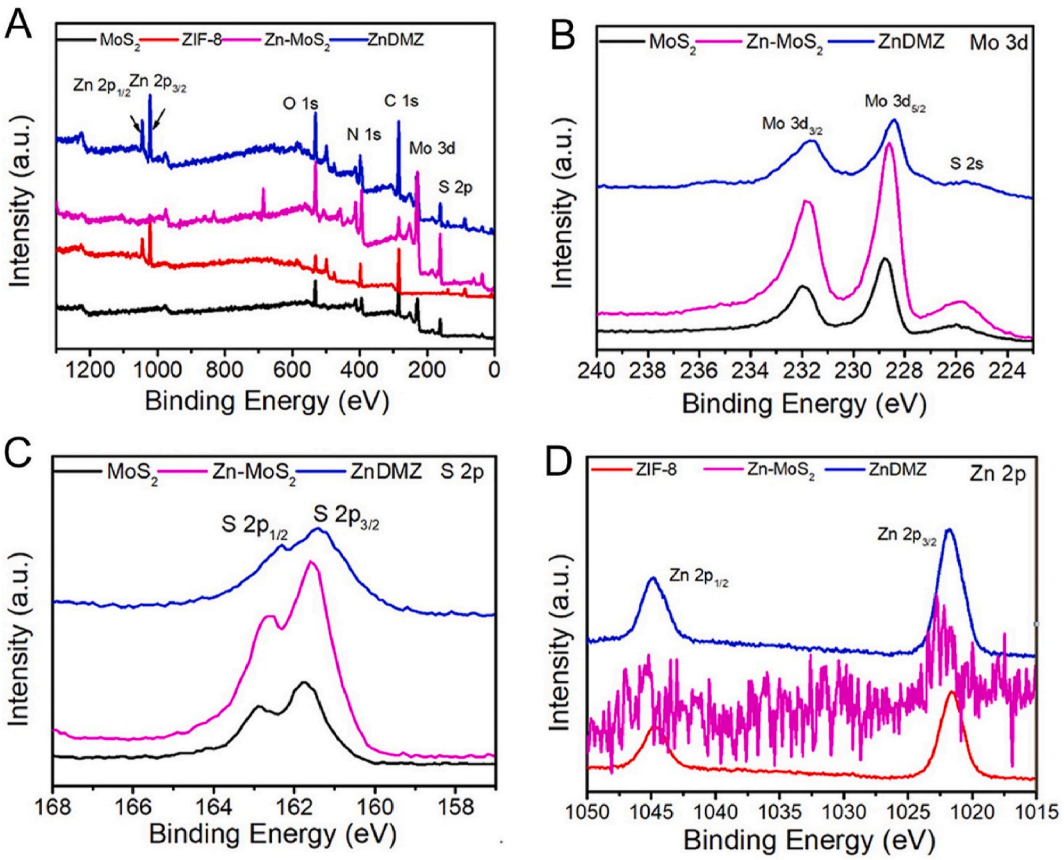

Fig. 2. X-ray photoelectron spectroscopy (XPS) spectra of (A) XPS survey spectra. (B) High-resolution XPS spectra of S 2p of MoS_2, Zn–MoS_2, ZnDMZ. (C) High-resolution XPS spectra of Mo 3d of MoS_2, Zn–MoS_2, ZnDMZ. (D) High-resolution XPS spectra of Zn 2p of ZIF-8, Zn–MoS_2, ZnDMZ.

light treatment, there was almost no change in the fluorescence intensity of DPBF in the control group, suggesting that pure 660 nm light irradiation does not generate $^1O_2$. Fig. S8b showed almost the same the fluorescence intensity of DPBF in ZIF-8 as the control group, indicating that ZIF-8 cannot produce $^1O_2$ under 660 nm light. In contrast, under the same condition, the fluorescence intensity of DPBF at 420 nm in MoS_2 group was greatly reduced (Fig. S8c), suggested that MoS_2 generated $^1O_2$ under visible light The Zn–MoS_2 (Fig. S8d) degrades more DPBF compared with MoS_2, indicating the Zn-doping improved the production of $^1O_2$. In contrast, ZnDMZ had a greater decrease in DPBF intensity compared to MoS_2 and Zn–MoS_2 (Fig. 3F), indicating the largest output of $^1O_2$ from ZnDMZ under the same condition. The contrast curve of $^1O_2$ tested by DPBF degradation (Fig. 3G) clearly indicated the strongest ability of ZnDMZ to produce $^1O_2$.

The photothermal property of the synthesized samples was shown in Fig. 3H. After 660 nm light irradiating for 20 min, the temperature of both the control group and ZIF-8 changed little, indicating that ZIF-8 had no photothermal effect under 660 nm light excitation. In contrast, after 6 min light irradiation, the temperature of MoS_2 group increased from room temperature (19 °C) to 50 °C, and finally maintains at 55.3 °C, indicating the excellent photothermal effect of MoS_2, which was ascribed to the parts of electrons photogenerated recombine with holes through inelastic collisions, resulting in lattice heat and thus temperature rise.[22] Zn-doping slightly weakened the photothermal effect of MoS_2 because the more photogenerated electrons transported to the surface of Zn with oxygen to from $^1O_2$. The ZnDMZ group showed almost the same photothermal curve as MoS_2, suggesting that the combination with ZIF-8 offset the loss caused by Zn-doping. The temperature rising and cooling profiles of ZnDMZ (Fig. 3I) disclosed that after three cycles ZnDMZ still maintained almost the same temperature rising and cooling profile, suggesting the excellent photothermal stability of the synthesized hybrid material.

3.3. Photocatalytic mechanism

The band gap of the synthesized materials can be calculated from UV–vis absorption curves. As shown in Fig. 4A, the band structure of MoS_2 (black curve) is calculated to be 1.58 eV and Zn-doping reduced the band gap of MoS_2 (pink curve) to be 1.38eV. More photogenerated electrons are generated under 660 nm light irradiation owning to the reduced band structure, thus promoting the ROS yield. The band gap of ZIF-8 is calculated to be 3.03 eV (red curve) cannot irradiation by 660 nm light. The band theory indicated that the work function (Φ) of samples affects the electron transfer behavior. The ultraviolet photoelectron spectroscopy (UPS) spectra of the different samples were utilized to calculate the Φ (Fig. 4B). The calculated Φ of MoS_2, Zn–MoS_2, ZIF-8, ZnDMZ is 5.20 eV, 4.95 eV, 4.22 eV, 4.39 eV, respectively. Obviously, MoS_2 have the largest Φ, while Zn–MoS_2 has a visible decline of Φ indicating that Zn-doping reduced the Φ of MoS_2. The ROS yields are closely related to the separation efficiency of photogenerated electron-hole pairs. Photogenerated electrons generally come from the inside and the surface of the material, and only the electrons on the surface can be captured by oxygen species to produce $^1O_2$. In other words, promoting the transportation of electrons from the inside of the material to the surface can surely enhances the effect of photocatalysis. Furthermore, reducing the surface work function of the materials can accelerate transportation of the electrons to the surface [37–39]. Compared to Zn–MoS_2, ZnDMZ has the lowest work function, this outcome suggests that the electrons from the ZnDMZ can easily arrive at the surface and floats freely between two materials. Since ZIF-8 is a semiconductor with good conductivity, when the electrons transport to the surface of MoS_2, the electrons would be conducted away by ZIF-8,

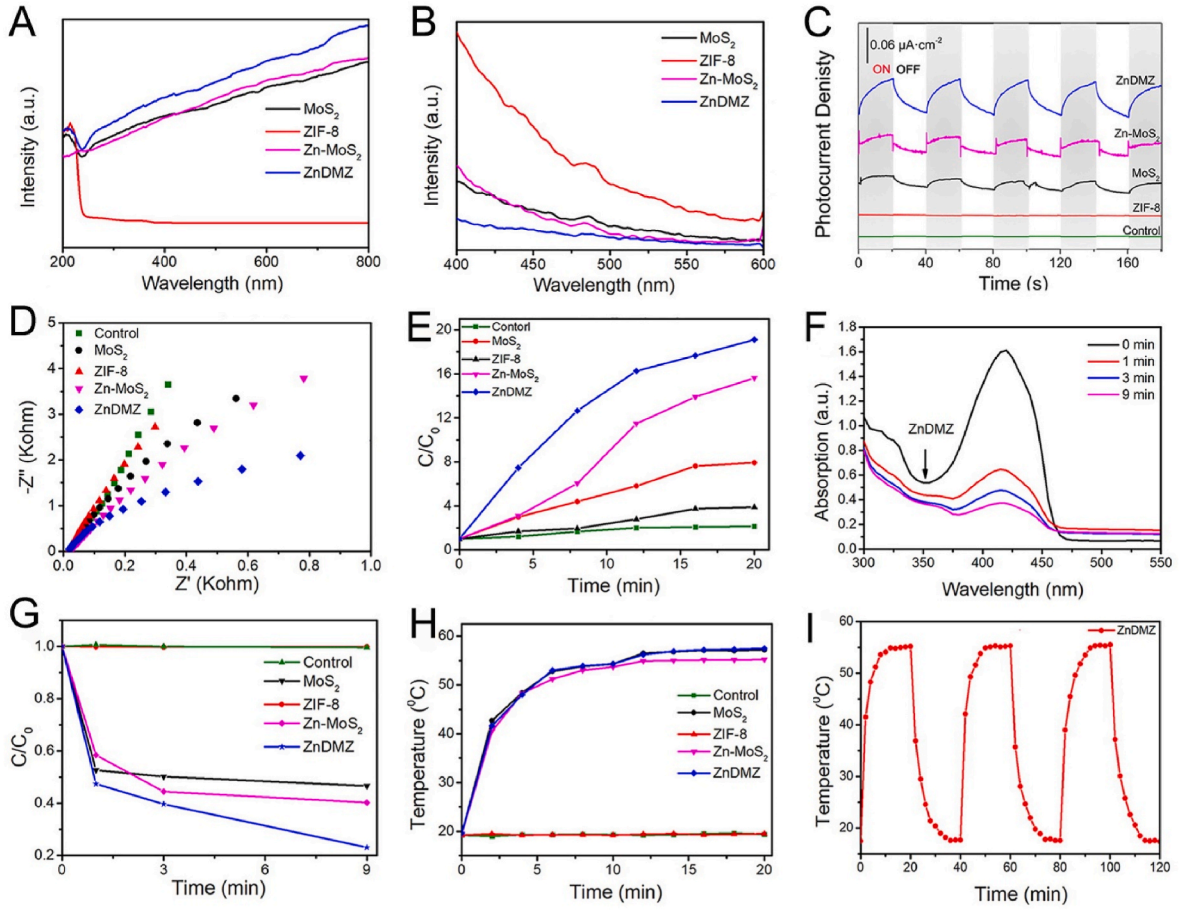

Fig. 3. Photocatalytic performance of different samples. (A) UV–visible absorption of different samples. (B) PL specture of different samples. (C) Photocurrent denisty of the samples. (D) EIS spectra of samples under 660 nm light irradiation. (E) ROS production with DCFH fluorescence probe under 660 nm light irradiation for 20 min. (F) The $^1O_2$ detected by degradation of DPBF of the materials under 660 nm light irradiation of ZnDMZ. (G) The contrast curve of $^1O_2$ tested by DPBF degradation. (H) Photothermal curves of different samples under 660 nm light irradiation for 20 min. (I) Temperature rising and cooling curves of ZnDMZ with and without 660 nm light irradiation.

further suppressing the recombination of electrons and holes so that the photocatalytic ability of MoS_2 can be effectively improved.

To illustrate the role of MOF in the charge transfer and capture O_2. Here, the DFT calculation simulation was used to in this work. (Fig. 4C–E). Since oxygen is an important factor in photocatalytic production of $^1O_2$, we calculated the ability of the materials to absorb and the position of O_2 (Fig. 4D). The O_2 absorption site is S atom for MoS_2, and the Zn is the site for oxygen absorption site for Zn–MoS_2. For ZIF-8 O_2 tends to adsorb on the nitrogen site of the imidazole ring, and O_2 on the heterojunction ZnDMZ also adsorbs on the N atom. The energy absorption of the samples was the ZnDMZ < ZIF-8<Zn–MoS_2<MoS_2, indicating that the heterojunction had a great ability to absorption oxygen. The charge density difference of Zn–MoS_2 and ZIF-8 was shown in Fig. 4E, electron accumulation (bule region) and depletion (yellow region) revealed the state of charge distribution at the interface. According to the planar-averaged electron, there are about 1.13×10^{-3} electron transfers at the interface. The electrons at the interface are exhausted at the ZIF-8 side (yellow region), making the part near the ZIF-8 positively charged, while accumulating at the Zn–MoS_2 side (bule region), making the part negatively charged. Therefore, a built-in electric field is formed at the interface, which can promote the separation of electrons and holes [40–42].

The mechanism of the photocatalytic production ROS is show in Fig. 4F. Before contact, according to the work function and the band structure, the conduction band (CB) and the valence band (VB) of MoS_2 was calculated as 0.44 eV, 2.02 eV *versus* the NHE respectively. After Zn doped MoS_2, the CB and VB of Zn–MoS_2 become −0.34 eV, 1.06 eV versus the NHE, respectively. Under 660 nm light, the electrons and holes of Zn–MoS_2 were separated, part of the electron jumped into CB and reacted with O_2, however, most of electrons fell back recombine with holes, resulting in poor photocatalytic effect. For ZIF-8, the CB and VB was calculated as −0.34 eV, 2.69 eV *versus* the NHE, respectively. The large band gap, resulting in ZIF-8 cannot be excited at 660 nm light. After contact, Zn–MoS_2 and ZIF-8 shared a Fermi energy level, which significantly contributed to the shift in the relative positions of the VB and CB. The position of CB of Zn–MoS_2 rose to −0.88 eV, while that of ZIF-8 fell to −0.40 eV. The CB of Zn–MoS_2 was higher than that of ZIF-8, so electrons on the CB of Zn–MoS_2 can be transferred to the CB of ZIF-8. The built-in electric field (yellow area) also speeds up electron migration. Therefore, the synergy of band offset and built-in electric field, photogenerated electron–hole pairs were effectively separated, which was the typical character of a P–N heterojunction. The $^1O_2$ generation production is closely related to electrons and holes ($O_2 + e^- \rightarrow O_2^{\bullet -} + h^+ \rightarrow {}^1O_2$) [43]. The CB of ZIF-8 (−0.40 eV) is higher than $O_2/O_2^{\bullet -}$ (−0.33 eV), indicated the oxygen can be converted to $O_2^{\bullet -}$ by electrons [44]. Then $O_2^{\bullet} -$ will change to $^1O_2$ in the VB position of Zn–MoS_2 under the action of holes. This process occurs continuously. In the summary, the reaction process can be described as follows: Oxygen is first adsorbed by MOF, and electrons and holes in Zn–MoS_2 are separated under 660 nm light excitation. Under the influence of the built-in electric field, the recombination of electrons and holes is inhibited, the adsorbed oxygen can be reduced under the action of electrons, and then reactive oxygen

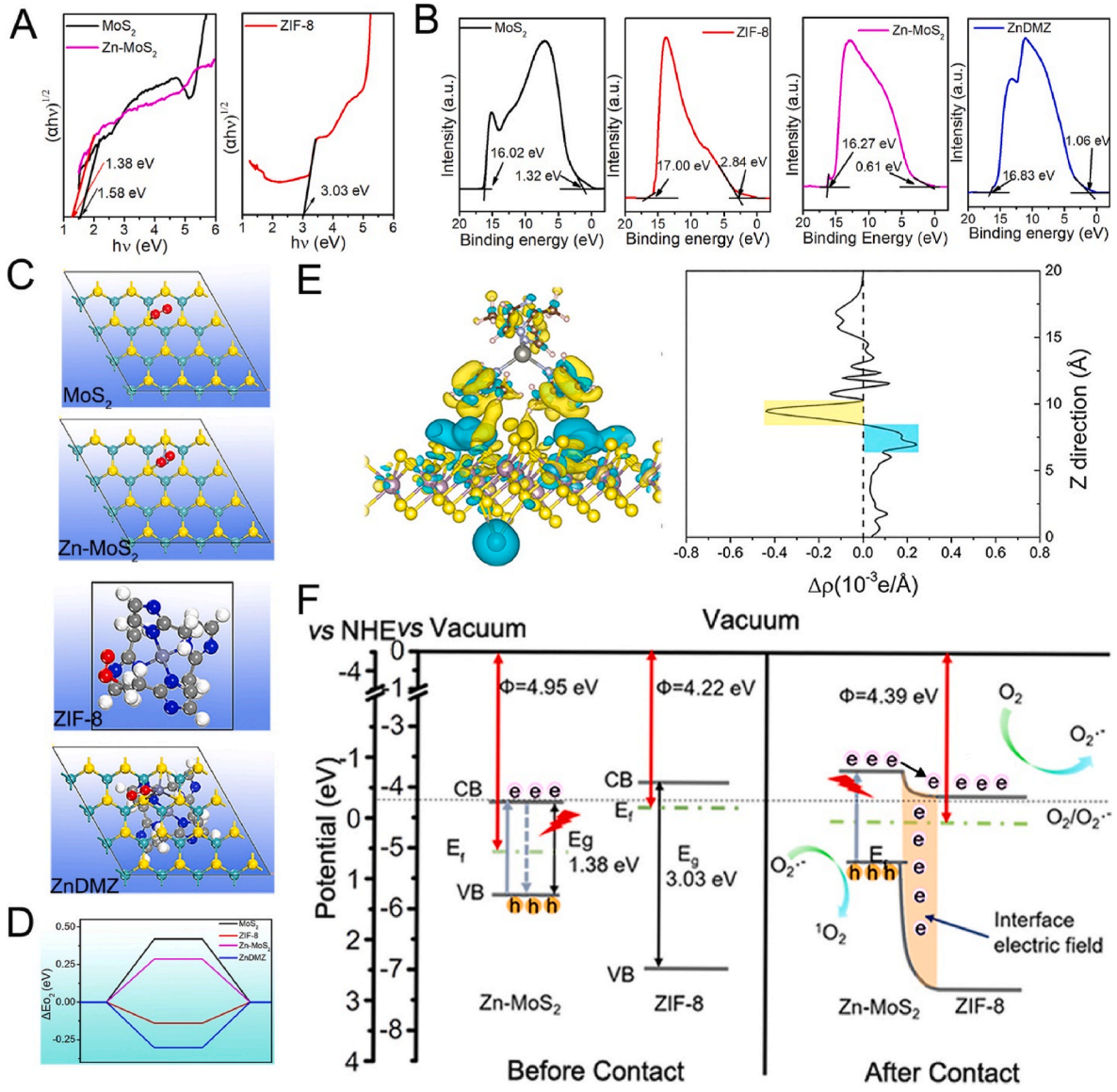

Fig. 4. The band structure calculated by UV–visible absorption specturm of (A) MoS_2, Zn–MoS_2, ZIF-8. Ultraviolet photoelectron spectroscopy (UPS) spectra of (B) MoS_2, ZIF-8, Zn–MoS_2, ZnDMZ. DFT theoretical calculation of MoS_2, ZIF-8, Zn–MoS_2, ZnDMZ. Absorption of Oxygen of (C) MoS_2, Zn–MoS_2, ZIF-8, ZnDMZ. (D) Adsorption energy of O_2 on the surfaces of MoS_2, ZIF-8, Zn–MoS_2, ZnDMZ. (E) 3D charge density difference of Zn doped MoS_2 and ZIF-8 heterojunction, where the bottom half belongs to MoS_2 and the top half belongs to ZIF-8. The yellow color represents electron depletion and the blue color represent the electron accumulation. $<\Delta\rho(z)>$ averaged through the xy plane of the layers corresponding to different locations along the z axis. (F) The photocatalyst mechanism schematic diagram of ZnDMZ P–N heterojunction under 660 nm light irradiation.

species are generated.

3.4. *In vitro antibacterial activity*

Spread plate method was used to detect the material's antibacterial ability. As shown in Fig. 5A, in comparison with the control group in the dark for 20 min, there was almost no change in the colony of all experimental groups under the same condition, suggesting little antibacterial activity of all materials in a short time in the dark In contrast, after irradiation under 660 nm light for 20 min, the bacterial colonies on the plate of the MoS_2 group, Zn–MoS_2 group and ZnDMZ immediately decreased compared to the control group, suggesting that both ZIF-8 and MoS_2 had some antibacterial activity under 660 nm light irradiation. Notably, only few scattered bacterial colonies appeared in ZnDMZ group, suggesting the highest antibacterial efficacy of ZnDMZ against *S. aureus*. The corresponding antibacterial efficacy was shown in Fig. 5B. The antibacterial efficacy of ZIF-8, MoS_2, Zn–MoS_2, ZnDMZ was 12.13%, 5.03%, 10.361%, 9.703%, respectively. ZIF-8 and ZnDMZ could release part of zinc ions, and zinc ions had bactericidal effect. Therefore, ZIF-8 and ZnDMZ groups showed certain bactericidal efficiency under dark conditions. After 660 nm light irradiation for 20 min, the antibacterial efficacy of the control group was close to zero, indicating no toxic effect of 20 min 660 nm light irradiation on bacteria. The antibacterial rate of the ZIF-8 group was 17.9754% under light irradiation, slightly higher than the one in the dark, indicating that light irradiation had a relatively small effect on ZIF-8 due to the slow release of Zn ions. The obvious enhancement of antibacterial efficacy of Zn–MoS_2 (69.87%) and MoS_2 (59.96%) was ascribed to the photothermal and photocatalytic effects excited by 660 nm light irradiation [22] ZnDMZ exhibited the highest antibacterial efficacy of 99.70%, which was to the synergistic effects of enhanced photocatalytic performance, hyperthermia and released Zn ions of the synthesized materials under 660 nm light irradiation.

Bacterial morphologies were further observed by FE-SEM to verify

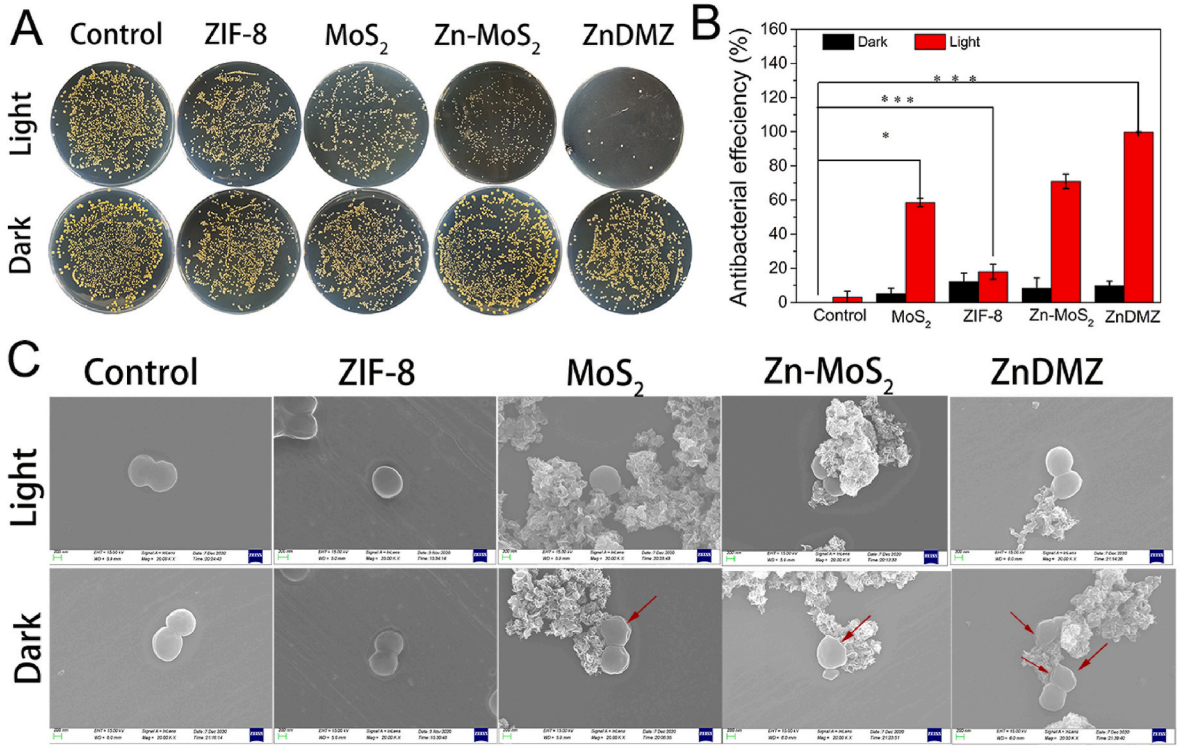

Fig. 5. The spread plate images of (A) *S. aureus* of the different materials with and without 660 nm light irradiation for 20 min. (B) The antibacterial efficiency of different samples, according to the spread plate pictures. (The error bars indicate means ± SD, n = 3. $*p < 0.05$, $**p < 0.01$, $***p < 0.001$). (C) The morphologies of *S. aureus* were observed by SEM of different samples.

the above antibacterial efficacy (Fig. 5C). In dark conditions, the bacteria in all groups were smooth and intact, indicating no damage of bacterial membrane. In contrast, after light irradiation, the membrane of bacteria in Zn–MoS_2 and ZnDMZ was seriously wrinkle and even broken (marked with red arrows), which was due to the damage of ROS and hyperthermia produced from the synthesized materials under light irradiation.

3.5. *In vitro cytocompatibility*

As an important cell line for wound healing, NIH-3T3 was used to evaluate the biocompatibility of materials. As shown in Fig. S9a, the three groups of MoS_2, Zn–MoS_2, and ZnDMZ showed good cytocompatibility, which was ascribed to the lamellar structure of MoS_2 because the nanosheet-like structure could provide enough active sites for the cell to spread and grow. The ZIF-8 exhibited obvious toxic effect on cells, which might be ascribed to the excess of released zinc ion [45]. Phototoxicity of the samples was measured with the light irradiation for 20 min. As shown in Fig. S9b, pure light was nontoxic to cells. In contrast, light irradiated MoS_2, Zn–MoS_2 and ZnDMZ showed a cell survival rate of 54.71%, 50.83% and 49.56%, respectively. The reduction was ascribed to the hyperthermia and ROS produced by the materials under light excitation, which killed the cells or weakened the activity of the cells. After 3 days of culturing, the cell viability rose up to over 80%, suggesting that the cytotoxicity caused by photothermal and ROS was reversible as culturing time increased. The fluorescence staining images of cells (Fig. S10) that the cells in the control group exhibited normal state with intact cytoplasm and nucleus. Compared with the control group, MoS_2, Zn–MoS_2 and ZnDMZ cells had more filopodia extending around, indicated that these three materials promoted cell growth, due to the nanosheet-like structure of MoS_2. In the case of Zn–MoS_2 and ZnDMZ, besides MoS_2, trace amount of zinc ion may be also affected the cell behaviors [46]. However, the large amount of release Zn ions induced the death of cells, which contributed to the shrink shape of cells in the group of ZIF-8. Fig. S11 was the release of Zinc ions of ZIF-8 and ZnDMZ. When MoS_2 is introduced, the release of zinc ions decreases obviously, which makes the toxicity of the material decrease significantly.

3.6. *Wound healing and biosafety*

The wound healing was evaluated by a model of mouse wounds with skin and the wound healing process at different time points were illustrated in Fig. 6A. After 10 days treatment, the wounds of the ZnDMZ-treated mouse were basically healed, while significant wounds of the Control group and 3 M group remained unhealed. As shown in Fig. 6B, the wound area was calculated and line chart was drawn. Group ZnDMZ had the best therapeutic effect in terms of wound healing trends, compared to group Control and group 3 M. After two days of treatment, all groups showed varying degrees of infection, as shown by GIMESE's stain (Fig. 6C). The number of bacteria in the wound treated with ZnDMZ was significantly lower than compared to other groups. And neutrophils, which are found in soft tissue, are an effective indicator of the degree of bacterial infection, the more neutrophils the greater the degree of bacterial infection. A 10-day H&E stain (Fig. 6D), could reveal the number of neutrophils at the wound site. The number of neutrophils in the control and 3 M groups were significantly higher than that in the ZnDMZ group. The above data could show that the treatment effect of ZnDMZ was the best. The staining analysis of heart, liver, spleen, lung and kidney (Fig. 6E) showed that after 10 days of treatment, no abnormalities were found in these major organs of mice, indicating that the synthesized materials were safe in the body.

4. Conclusion

In this work, we successfully prepared MOF-based heterojunction, which has good bacteria-clearing effect under 660 nm light excitation. In addition, this synthesized material also has good biocompatibility and

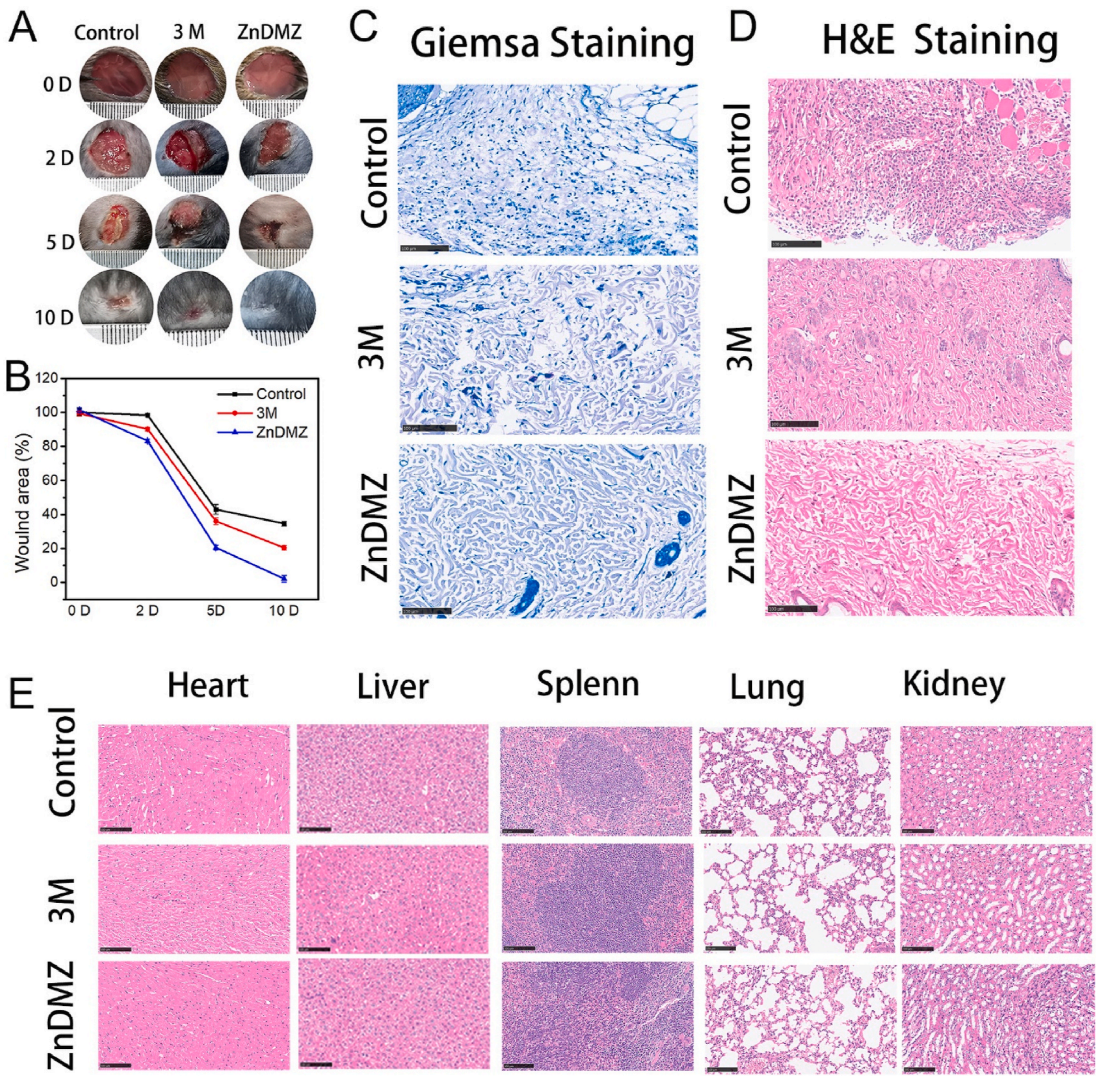

Fig. 6. (A) The actual image of wound sizes of Control group, 3 M group, and ZnDMZ group with 660 nm light of 0, 2, 5, and 10 days. (B) Wound area changes statistics of different samples with different days. (C) Giemsa staining for residual bacterial detection in reconstructed skin tissues in two days, scale bar = 100 μm. (D) H&E staining for histological analysis of the reconstructed skin tissues in 10 days, scale bar = 100 μm. (E) H&E staining images of heart, liver, spleen, lung, and kidney of rats are obtained by H&E staining after 10 days.

wound healing effect. The work function of the prepared nanosheet-like MoS_2 is reduced by zinc ion doping, and the separation of electrons and holes is better promoted. Basically, the introduction of MOF can not only form a built-in electric field at the interface to further promote the separation efficiency of photogenerated electron-hole pairs, but also increase the adsorption of oxygen species, which provides more favorable places for the generation of singlet states. Consequently, it will strengthen the photodynamic therapeutic effects to kill bacteria and eliminate infection. This work utilizes the technique of Zn-doping to reduce the work function of semiconductor and then constructs a heterostructured hybrid by utilizing the work function difference between the electroconductive MOF and Zn-doped MoS_2, which endows the synthesized materials with powerful antibacterial ability and wounds healing ability. The current study will provide new insight for developing not only MOF-based photo-excited bacteria-killing materials, but also photo-electrical devices such as solar cell modules and photoelectric sensors.

CRediT authorship contribution statement

C. W., X. L. and S. W. conceived the research and designed all the experiments. C. W. and Y. L. carried out the experiments. C. W., Y. L., Z. C., Z. L., J.L., Y.Z., Y. L., X. F. and S. Z. performed the analysis of experimental data. C. W., X. L. and S. W. wrote the paper. All authors have approved the final manuscript.

CRediT authorship contribution statement

Chaofeng Wang: Conceptualization, Methodology, Writing – original draft, Data curation, Investigation. **Yue Luo:** Methodology, Visualization. **Xiangmei Liu:** Conceptualization, Writing – review & editing, Supervision, Project administration. **Zhenduo Cui:** Methodology. **Yufeng Zheng:** Methodology, Visualization. **Yanqin Liang:** Methodology. **Zhaoyang Li:** Visualization. **Shengli Zhu:** Visualization. **Jie Lei:** Visualization. **Xiaobo Feng:** Visualization. **Shuilin Wu:** Conceptualization, Writing – review & editing, Supervision, Project administration, Funding acquisition.

Declaration of competing interest

The authors declare that they have no known competing financial interests or personal relationships that could have appeared to influence

the work reported in this paper.

Acknowledgments

This work is jointly supported by the China National Funds for Distinguished Young Scientists (no.51925104), and the National Natural Science Foundation of China (nos. 51871162, 5217130333). The authors thank Wuhan Union Hospital also for their collaboration and assistance with this animal experiments.

Appendix A. Supplementary data

Supplementary data to this article can be found online at https://doi.org/10.1016/j.bioactmat.2021.10.033.

References

[1] Z. Xu, S. Han, Z. Gu, J. Wu, Advances and impact of antioxidant hydrogel in chronic wound healing, Adv. Healthc. Mater. 9 (5) (2020) 1901502.
[2] L. Shi, X. Liu, W. Wang, L. Jiang, S. Wang, A self-pumping dressing for draining excessive biofluid around wounds, Adv. Mater. 31 (5) (2019) 1804187.
[3] J. Zhou, D. Yao, Z. Qian, S. Hou, L. Li, A.T.A. Jenkins, Y. Fan, Bacteria-responsive intelligent wound dressing: simultaneous in situ detection and inhibition of bacterial infection for accelerated wound healing, Biomaterials 161 (2018) 11–23.
[4] S.L. Percival, C. Emanuel, K.F. Cutting, D.W. Williams, Microbiology of the skin and the role of biofilms in infection, Int. Wound J. 9 (1) (2012) 14–32.
[5] X. Lei, L. Qiu, M. Lan, X. Du, S. Zhou, P. Cui, R. Zheng, P. Jiang, J. Wang, J. Xia, Antibacterial photodynamic peptides for *Staphylococcal* skin infection, Biomater. Sci. 8 (23) (2020) 6695–6702.
[6] Y. Yu, L. Tan, Z. Li, X. Liu, Y. Zheng, X. Feng, Y. Liang, Z. Cui, S. Zhu, S. Wu, Single-atom catalysis for efficient sonodynamic therapy of methicillin-resistant *Staphylococcus aureus*-infected osteomyelitis, ACS Nano 15 (6) (2021) 10628–10639.
[7] E.P. Martínez, G.C. Monzón, Daptomycin plus fosfomycin versus daptomycin alone for methicillin-resistant *Staphylococcus aureus* severe infection: post hoc analysis is warranted, Clin. Infect. Dis. 72 (11) (2020) e922-e922.
[8] J.K. Martin II, J.P. Sheehan, B.P. Bratton, G.M. Moore, A. Mateus, S.H.J. Li, H. Kim, J.D. Rabinowitz, A. Typas, M.M. Savitski, M.Z. Wilson, Z. Gitai, A dual-mechanism antibiotic kills gram-negative bacteria and avoids drug resistance, Cell 181 (7) (2020) 1518–1532.
[9] Y. Huang, Q. Gao, X. Li, Y. Gao, H. Han, Q. Jin, K. Yao, J. Ji, Ofloxacin loaded MoS_2 nanoflakes for synergistic mild-temperature photothermal/antibiotic therapy with reduced drug resistance of bacteria, Nano Res 13 (2020) 2340–2350.
[10] R. Yang, G. Song, L. Wang, Z. Yang, J. Zhang, X. Zhang, S. Wang, L.H. Ding, N. Ren, A. Wang, X. Yu, Full solar-spectrum-driven antibacterial therapy over hierarchical Sn_3O_4/PDINH with enhanced photocatalytic activity, Small 17 (39) (2021), e2102744.
[11] Q. Guan, L.L. Zhou, Y.A. Li, W.Y. Li, S. Wang, C. Song, Y.B. Dong, Nanoscale covalent organic framework for combinatorial antitumor photodynamic and photothermal therapy, ACS Nano 13 (11) (2019) 13304–13316.
[12] D. Han, P. Yu, X. Liu, Y. Xu, S. Wu, Polydopamine modified CuS@HKUST for rapid sterilization through enhanced photothermal property and photocatalytic ability, Rare Met. (2021), https://doi.org/10.1007/s12598-021-01786-1.
[13] Y. Li, X. Liu, L. Tan, Z. Cui, D. Jing, X. Yang, Z. Li, S. Zhu, Y. Zheng, K.W.K. Yeung, D. Zheng, X. Wang, S. Wu, Eradicating multidrug-resistant bacteria rapidly using a multi-functional g-C_3N_4@Bi_2S_3 nanorod heterojunction with or without antibiotics, Adv. Funct. Mater. 29 (20) (2019) 1900946.
[14] L. Pan, M. Ai, C. Huang, L. Yin, X. Liu, R. Zhang, S. Wang, Z. Jiang, X. Zhang, J. J. Zou, W. Mi, Manipulating spin polarization of titanium dioxide for efficient photocatalysis, Nat. Commun. 11 (1) (2020) 1–9.
[15] R. Lv, Y. Liang, Z. Li, S. Zhu, Z. Cui, S. Wu, Flower-like CuS/Graphene oxide with photothermal and enhanced photocatalytic effect for rapid bacteria-killing using visible light, Rare Met. (2021), https://doi.org/10.1007/s12598-021-01759-4.
[16] Z. Yuan, B. Tao, Y. He, J. Liu, C. Lin, X. Shen, Y. Ding, Y. Yu, C. Mu, P. Liu, K. Cai, Biocompatible MoS_2/PDA-RGD coating on titanium implant with antibacterial property *via* Intrinsic ROS-independent oxidative stress and NIR irradiation, Biomaterials 217 (2019) 119290.
[17] L. Yan, J. Mu, P. Ma, Q. Li, P. Yin, X. Liu, Y. Cai, H. Yu, J. Liu, G. Wang, A. Liu, Gold nanoplates with superb photothermal efficiency and peroxidase-like activity for rapid and synergistic antibacterial therapy, Chem. Commun. 57 (9) (2021) 1133–1136.
[18] W. Yin, J. Yu, F. Lv, L. Yan, L.R. Zheng, Z. Gu, Y. Zhao, Functionalized nano-MoS_2 with peroxidase catalytic and Near-Infrared photothermal activities for safe and synergetic wound antibacterial applications, ACS Nano 10 (12) (2018) 11000–11011.
[19] L. Zhu, J. Ji, J. Liu, S. Mine, M. Matsuoka, J. Zhang, M. Xing, Designing 3D-MoS_2 sponge as excellent cocatalysts in advanced oxidation processes for pollutant control, Angew. Chem. Int. Ed. 59 (33) (2020) 13968–13976.
[20] H. Wang, X. Xiao, S. Liu, C.L. Chiang, X. Kuai, C.K. Peng, Y.C. Lin, X. Meng, J. Zhao, J. Choi, Y.G. Lin, J.M. Lee, L. Gao, Structural and electronic optimization of MoS_2 edges for hydrogen evolution, J. Am. Chem. Soc. 141 (46) (2019) 18578–18584.
[21] S. Li, Y. Liu, X. Zhao, Q. Shen, W. Zhao, Q. Tan, N. Zhang, P. Li, L. Jiao, X. Qu, Sandwich-like heterostructures of MoS_2/Graphene with enlarged interlayer spacing and enhanced hydrophilicity as high-performance cathodes for aqueous zinc-ion batteries, Adv. Mater. 33 (12) (2021) 2007480.
[22] M. Zhu, X. Liu, L. Tan, Z. Cui, Y. Liang, Z. Li, K.W.K. Yeung, S. Wu, Photo-responsive chitosan/Ag/MoS_2 for rapid bacteria-killing, J. Hazard Mater. 383 (2020) 121122.
[23] R. Zhang, X. Ma, C. An, D. Zhang, D. Sun, X. Hu, J. Liu, Self-powered photodetector based on vertical MoO_3/MoS_2 hetero-structure with gate tunable photo-response, 2D Mater. 6 (3) (2019), 035033.
[24] Z. Zhang, W. Li, Y. Liu, Z. Yang, L. Ma, H. Zhuang, E. Wang, C. Wu, Z. Huan, F. Guo, J. Chang, Design of a biofluid-absorbing bioactive sandwich-structured Zn-Si bio-ceramic composite wound dressing for hair follicle regeneration and skin born wound healing, Bioact. Mater. 6 (7) (2021) 1910–1920.
[25] J. Xiao, Y. Zhu, S. Huddleston, P. Li, B. Xiao, O.K. Farha, G.A. Ameer, Copper metal-organic framework nanoparticles stabilized with folic acid improve wound healing in diabetes, ACS Nano 12 (2) (2018) 1023–1032.
[26] P. Najmi, N. Keshmiri, M. Ramezanzadeh, B. Ramezanzadeh, Synthesis and application of Zn-doped polyaniline modified multi-walled carbon nanotubes as stimuli-responsive nanocarrier in the epoxy matrix for achieving excellent barrier-self-healing corrosion protection potency, Chem. Eng. J. 412 (2021) 128637.
[27] Q. Wang, P. Wang, P. Xu, Y. Li, J. Duan, G. Zhang, L. Hu, X. Wang, W. Zhang, Visible-light-driven photo-Fenton reactions using $Zn_{1-1.5x}Fe_xS$/g-C_3N_4 photocatalyst: degradation kinetics and mechanisms analysis, Appl. Catal., B 266 (2020) 118653.
[28] J. Li, X. Liu, L. Tan, Z. Cui, X. Yang, Y. Liang, Z. Li, S. Zhu, Y. Zheng, K.W.K. Yeung, X. Wang, S. Wu, Zinc-doped Prussian blue enhances photothermal clearance of Staphylococcus aureus and promotes tissue repair in infected wounds, Nat. Commun. 10 (1) (2019) 1–15.
[29] Y. Li, X. Liu, L. Tan, Z. Cui, X. Yang, Y. Zheng, K.W.K. Yeung, P.K. Chu, S. Wu, Rapid sterilization and accelerated wound healing using Zn^{2+} and graphene oxide modified g-C_3N_4 under dual light irradiation, Adv. Funct. Mater. 28 (30) (2018) 1800299.
[30] M. Deng, Z. Li, X. Rong, Y. Luo, B. Li, L. Zheng, X. Wang, F. Lin, A.J. Meixner, K. Braun, X. Zhu, Z. Fang, Light-controlled near-field energy transfer in plasmonic metasurface coupled MoS_2 monolayer, Small 16 (40) (2020) 2003539.
[31] Y. Su, L. Zhang, W. Wang, X. Li, Y. Zhang, D. Shao, Enhanced H_2 evolution based on ultrasound-assisted piezo-catalysis of modified MoS_2, J. Mater. Chem. 6 (25) (2018) 11909–11915.
[32] P. Liu, J. Zhu, J. Zhang, K. Tao, D. Gao, P. Xi, Active basal plane catalytic activity and conductivity in Zn doped MoS_2 nanosheets for efficient hydrogen evolution, Electrochim. Acta 260 (2018) 24–30.
[33] Y. Zhang, S.J. Park, Facile construction of MoO_3@ ZIF-8 core-shell nanorods for efficient photoreduction of aqueous Cr (VI), Appl. Catal. B Environ. 240 (2019) 92–101.
[34] Y. Yao, H. Hu, H. Zheng, F. Wei, M. Gao, Y. Zhang, S. Wang, Zn-MoS_2 nanocatalysts anchored in porous membrane for accelerated catalytic conversion of water contaminants, Chem. Eng. J. 398 (2020) 125455.
[35] G. Yilmaz, T. Yang, Y. Du, X. Yu, Y.P. Feng, L. Shen, G.W. Ho, Stimulated electrocatalytic hydrogen evolution activity of MOF-derived MoS_2 basal domains via charge injection through surface functionalization and heteroatom doping, Adv. Sci. 6 (15) (2019) 1900140.
[36] J. Qiu, X.F. Zhang, X. Zhang, Y. Feng, Y. Li, L. Yang, L. Yang, H. Lu, J. Yao, Constructing $Cd_{0.5}Zn_{0.5}S$@ZIF-8 nanocomposites through self-assembly strategy to enhance Cr (VI) photocatalytic reduction, J. Hazard Mater. 349 (2018) 234–241.
[37] Q. Meng, C. Lv, J. Sun, W. Hong, W. Xing, L. Qiang, J. Chen, X. Jin, High-efficiency Fe-Mediated Bi_2MoO_6 nitrogen-fixing photocatalyst: reduced Surface work function and ameliorated surface reaction, Appl. Catal. B Environ. 256 (2019) 117781.
[38] Q. Liang, X. Liu, J. Wang, Y. Liu, Z. Liu, L. Tang, B. Shao, W. Zhang, S. Gong, M. Cheng, Q. He, C. Feng, In-situ self-assembly construction of hollow tubular g-C_3N_4 isotype heterojunction for enhanced visible-light photocatalysis: experiments and theories, J. Hazard Mater. 401 (2021) 123355.
[39] B. Sun, W. Zhou, H. Li, L. Ren, P. Qiao, W. Li, H. Fu, Synthesis of particulate hierarchical tandem heterojunctions toward optimized photocatalytic hydrogen production, Adv. Mater. 30 (43) (2018) 1804282.
[40] Y.J. Yuan, Z.K. Shen, S. Song, J. Guan, L. Bao, L. Pei, S. Wu, W. Bai, Z. Yu, Z. Ji, Z. Zou, Co-P bonds as atomic-level charge transfer channel to boost photocatalytic H_2 production of Co_2P/Black phosphorus nanosheets photocatalyst, ACS Catal. 9 (9) (2019) 7801–7807.
[41] C. Mao, W. Zhu, Y. Xiang, Y. Zhu, J. Shen, X. Liu, S. Wu, K.M. Cheung, K.W. K. Yeung, Enhanced near-infrared photocatalytic eradication of MRSA biofilms and osseointegration using oxide perovskite-based P-N heterojunction, Adv. Sci. 8 (2021), e2002211.
[42] C. Dong, Y. Bao, T. Sheng, Q. Yi, Q. Zhu, B. Shen, M. Xing, I.M. Lo, J. Zhang, Singlet oxygen triggered by robust bimetallic MoFe/TiO_2 nanospheres of highly efficacy in solar-light-driven peroxymonosulfate activation for organic pollutants removal, Appl. Catal. B Environ. 286 (2021), e119930.
[43] D. Li, M. Chen, Z. Sun, P. Yu, Z. Liu, P.M. Ajayan, Z. Zhang, Two-dimensional non-volatile programmable P-N junctions, Nat. Nanotechnol. 12 (9) (2017) 901–906.

[44] Y. Nosaka, A.Y. Nosaka, Generation and detection of reactive oxygen species in photocatalysis, Chem. Rev. 117 (17) (2017) 11302–11336.
[45] S. Wang, K. Li, Y. Chen, H. Chen, M. Ma, J. Feng, Q. Zhao, J. Shi, Biocompatible PEGylated MoS_2 nanosheets: controllable bottom-up synthesis and highly efficient photothermal regression of tumor, Biomaterials 39 (2015) 206–217.
[46] X. Yao, G. Zhu, P. Zhu, J. Ma, W. Chen, Z. Liu, T. Kong, Omniphobic ZIF-8@ hydrogel membrane by microfluidic-emulsion-templating method for wound healing, Adv. Funct. Mater. 30 (13) (2020) 1909389.